Journal of Optics

ACCEPTED MANUSCRIPT

Multiple compound Tamm waves with Uller-Zenneck wave characteristics guided by dissipative dielectric defect in periodic multilayered isotropic dielectric material

To cite this article before publication: Muhammad Danyal *et al* 2019 *J. Opt.* in press https://doi.org/10.1088/2040-8986/ab1462

Multiple compound Tamm waves with Uller-Zenneck wave characteristics guided by dissipative dielectric defect in periodic multilayered isotropic dielectric material

Muhammad Danyal[1], Husnul Maab[1*], Arbab Abdur Rahim[1], and Muhammad Mahmood Ali[1,2]

[1]Faculty of Electrical Engineering, GIK Institute of Engineering Sciences and Technology, Topi 23640, Pakistan
[2] Department of Electronic and Computer Engineering, Optical Fibre Sensors Research Centre, University of Limerick, Limerick Ireland
*Corresponding author: maab@giki.edu.pk

Abstract. A canonical problem configured in three different arrangements of periodic multilayered isotropic dielectric material's layers with a dissipative dielectric defect, to guide multiple compound Tamm waves with Uller-Zenneck wave characteristics, was formulated and solved. The numerical solutions showed multiple Tamm waves guided at a fixed wavelength along the disspative defect with same polarization state. These waves propagate with different phase speeds, different propagation distances, different field localizations, and different field profiles. The results identified excitation of symmetric and anti-symmetric solutions of *p*-polarized Tamm waves and *p*- and *s*-polarized waveguide modes. The high phase speed solutions ceased to exist beyond certain limit of dissipative dielectric defect thickness, but the low phase speed solutions were computed for a wide range of dissipative dielectric defect thickness. The Tamm waves were compounded when the thickness of defect is very small and transmuted into waveguide modes for increasing thickness of dissipative dielectric defect because most of the energy is then strongly confined to the dissipative dielectric defect. The excitation of multiple Tamm waves and waveguide modes at a given dissipative dielectric defect thickness and fixed wavelength can be considered for multi-channel optical communication and sensing applications.

1. Introduction

In 1902, Wood [1] observed anomalous dark bands by illuminating metallic gratings. These anomalies were theoretically studied by Fano [2] and associated them to the excitation of surface electromagnetic waves (SEWs). SEWs are electromagnetic waves which are strongly or loosely bounded with the interface between two dissimilar materials and attenuate exponentially perpendicular to the plane of interface. The SEWs is known as surface plasmon-polariton (SPP) wave when excited at the interface between a metal and a homogeneous and isotropic dielectric material [3, 4]. The first successful experimental excitation of SPP wave was accomplished by works of Otto [5], Krestchmann and Raether [6] in 1968. Most common application of SPP wave is surface plasmon resonance (SPR) sensor [3, 4, 7, 8, 9]. The SPR sensor's operation depends on change in refractive index of dielectric analyte placed on top of a metal

which cause a changing effect in optical properties of optical signal interacting with the SPP wave. Hence, SPR sensors are characterized by change in one of the following characteristics of light; angle, intensity, wavelength, phase, and/or polarization.

In the first decade of 20th century, Uller [10] and Zenneck [11] proposed the theoretical prediction of SEWs propagation guided at the interface of air and sea water/ground in the microwave regime. Later, the rigorous mathematical analysis of similar waves was done by Sommerfeld [12, 13]. By combining the concepts of Uller and Zenneck, a new kind of SEW was theoretically investigated at the interface between two dissimilar dielectric materials of which one partnering material essentially be dissipative. This new type of SEW was named Uller-Zenneck wave [14, 15]. The Uller-Zenneck waves in radio-frequency regime are conveniently excited if the incident plane wave is highly oblique. However, the excited wave is in ambiguity with other kinds of waves at radio frequencies [16]. This problem is partially attributed to the Brewster phenomenon [17, 18]. For finite thickness of partnering materials and under optical illumination, Uller-Zenneck waves are not excited at the planar interface. However, these waves are excited when the interface is periodically corrugated [19]. Uller-Zenneck waves are characterized by phase speed higher than the phase speed of incident plane wave.

An earlier study of compound SPP waves guided along the metal slab sandwiched into two isotropic homogeneous dielectric materials showed long propagation distance as compared to SPP waves at single interface. However, these waves decoupled when the slab thickness becomes sufficiently larger than the skin depth of metal [20]. In this regard, compound guided waves (CGWs) propagation guided by metallic slab sandwiched between a homogeneous isotropic dielectric and a periodic multilayered isotropic dielectric (PMLID) material or a structurally chiral material were provided [21, 22]. Similarly, planar interface structures were suggested that support CGWs which mix the characteristics of various types of SEWs e.g. SPP waves, Tamm waves [23], Dyakonov-Tamm waves [24], and Uller-Zenneck waves [25]. The excitation of SPP and Uller-Zenneck waves leads to smaller propagation distance in the direction of propagation because of a lossy partnering material. As compared to SPP and Uller-Zenneck waves, Tamm waves [23] on the other hand–which exist at the interface of two isotropic dielectric materials with at least one partnering material having nonhomogeneity in the direction normal to the interface–propagate upto long distances and undergo small attenuation because of lossless partnering materials. The experimental excitation of Tamm waves in 1978 [26] led to its applications in optical sensing [7, 8]. Keeping in view the aforementioned discussion, it was decided to investigate multiple compound Tamm waves with Uller-Zenneck wave characteristics propagation guided along the dissipative dielectric defect in PMLID material. The problem was further investigated for multiple compound Tamm waves with Uller-Zenneck wave characteristics propagation in three different configurations as shown in Fig.1. The lay out of the paper is as under.

Section 2 comprises the construction of canonical boundary value problem and its variants. Numerical results are provided in Section 3 and the concluding remarks are given in Section 4. Time dependence of $\exp(-i\omega t)$ is implicit. Vectors are square bracketed $[\cdot]$ while square matrices are double underlined and square bracketed $[\underline{\underline{\cdot}}]$. The free space permittivity and permeability are denoted by ε_0 and μ_0. The free space wavenumber, the free space wavelength and the intrinsic impedance are represented by $k_0 = \omega\sqrt{\mu_0\varepsilon_0}$, $\lambda_0 = 2\pi/k_0$, and $\eta_0 = \sqrt{\mu_0/\varepsilon_0}$, respectively. The Cartesian coordinate unit vectors are denoted by $\hat{u}_x, \hat{u}_y,$ and $\hat{u}_z$. The vector transpose operation is denoted

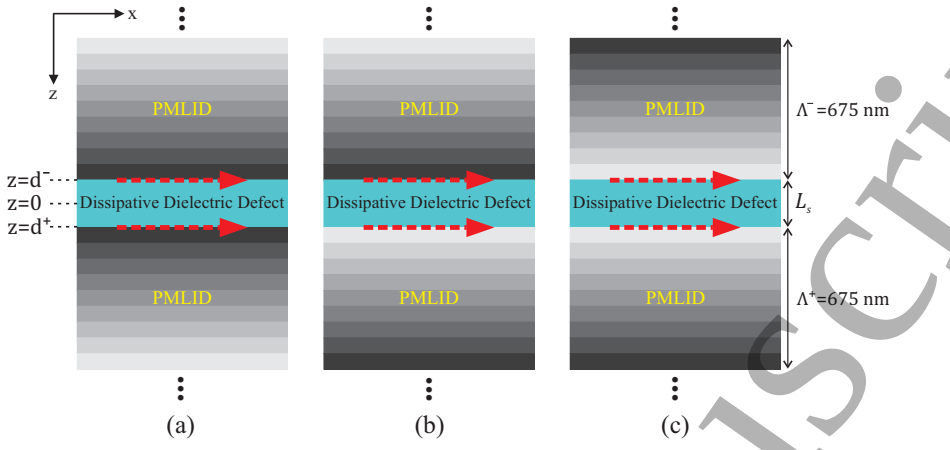

Figure 1. Schematic of canonical problem shows propagation of Tamm waves with Uller-Zenneck wave characteristic (red dashed arrow) at the interfaces of dissipative dielectric defect in PMLID material. The three problems can be differentiated as: (a) layers $j = 1$ (given in Table 1) of upper and lower PMLID are nearest to dissipative dielectric defect interfaces; (b) layer $j = 1$ (given in Table 1) of upper PMLID and layer $j = 9$ (given in Table 1) of lower PMLID are nearest to dissipative dielectric defect interfaces; (c) layers $j = 9$ (given in Table 1) of upper and lower PMLID are nearest to dissipative dielectric defect interfaces.

by $[\cdot]^T$.

2. Problem statement

Let consider the canonical problem shown in Fig. 1, region ($d^- < z < d^+$) represents dissipative dielectric defect of thickness ($L_s = d^+ - d^-$) with relative permittivity ε_d. The half-spaces ($z < d^-$) and ($z > d^+$) represent non-dissipative periodic multilayered isotropic dielectric (PMLID) materials with a period $\Lambda^{\pm} = 675$nm. A single period of PMLID material is comprised of nine layers of silicon oxynitrides [27] each of thickness $d = 75$nm. PMLID can be fabricated using plasma enhanced chemical vapor deposition (CVD) in the presence of a specific composition of silane, ammonia, and nitrous oxide [27, 25]. The relative permittivities and the corresponding refractive indexes of each layer of PMLID material for one period are tabulated in Table 1. In Fig. 1, the deep dark colored layer represents highest value of relative permittivity ($j = 1$) while the lighter dark colored layer represents smallest value of relative permittivity ($j = 9$) of PMLID material.

The problem is investigated for multiple compound Tamm waves with Uller-Zenneck wave characteristics [25] for three different cases. The schematic diagrams of these cases are shown in Fig. 1(a), Fig. 1(b), and Fig. 1(c).

- In Fig. 1(a), the permittivities of PMLID material layers in each period above and below the dielectric defect interfaces are arranged in descending order. Hence, it represents symmetrical pattern of PMLID material layers permittivities with respect to the dielectric defect. In this case, the highest permittivity layer $j = 1$ of PMLID material is closest to the both interfaces of the dielectric defect.
- In Fig. 1(b), the permittivities of PMLID material layers in each period above and below the dielectric defect interfaces are arranged in ascending and descending

Table 1. Representative relative permittivity ε_j of nine different dielectric layers of PMLID material and their corresponding $n_j^2 = \varepsilon_j$ refractive index values at free space wavelength $\lambda_\circ = 633$nm [27].

j	ε_j	n_j
1	3.9357	1.9839
2	3.3033	1.8175
3	3.1515	1.7752
4	3.0056	1.7337
5	2.7526	1.6591
6	2.6143	1.6169
7	2.4475	1.5644
8	2.3161	1.5219
9	2.1837	1.4777

orders, respectively. Hence, it represents asymmetrical pattern of PMLID material layers permittivities with respect to the dielectric defect. In this case, the highest permittivity layer $j = 1$ and lowest permittivity layer $j = 9$ of PMLID material are closest to $z = d^-$ and $z = d^+$ interfaces of the dielectric defect, respectively.

- In Fig. 1(c), the permittivities of PMLID material layers in each period above and below the dielectric defect interfaces are arranged in ascending order. Hence, it again represents symmetrical pattern of PMLID material layers permittivities with respect to the dielectric defect. In this case, the lowest permittivity layer $j = 9$ of PMLID material is closest to both the interfaces of the dielectric defect.

Without any loss of generality, let the electric and magnetic field phasors $\mathbf{E}(\mathbf{r}) = \mathbf{e}(z)e^{i\kappa x}$ and $\mathbf{H}(\mathbf{r}) = \mathbf{h}(z)e^{i\kappa x}$ of excited Tamm wave propagate along x-direction in xz-plane. By substituting the electric and magnetic field phasors in the frequency domain source-free Maxwell's curl postulates result in the following three matrix ordinary differential equations

$$\frac{d}{dz}[\mathbf{f}(z)] = i\begin{cases} [\underline{\underline{G}}_j^-(z)]\cdot[\mathbf{f}(z)]\,, & z < d^-\,, \\ [\underline{\underline{G}}^D]\cdot[\mathbf{f}(z)]\,, & d^- \le z \le d^+\,, \\ [\underline{\underline{G}}_j^+(z)]\cdot[\mathbf{f}(z)]\,, & z > d^+\,, \end{cases} \tag{1}$$

where $j \in [1, 9]$, the column vector $[\mathbf{f}(z)] = [e_x(z) \;\; e_y(z) \;\; h_x(z) \;\; h_y(z)]^T$, and the 4×4 square matrices are

$$[\underline{\underline{G}}_j^{\pm}(z)] = \begin{bmatrix} 0 & 0 & 0 & \omega\mu_0 - \frac{\kappa^2}{\omega\varepsilon_0\varepsilon_j^{\pm}(z)} \\ 0 & 0 & -\omega\mu_0 & 0 \\ 0 & -\omega\varepsilon_0\varepsilon_j^{\pm}(z) + \frac{\kappa^2}{\omega\mu_0} & 0 & 0 \\ \omega\varepsilon_0\varepsilon_j^{\pm}(z) & 0 & 0 & 0 \end{bmatrix},$$

$$[\underline{\underline{G}}^D] = \begin{bmatrix} 0 & 0 & 0 & \omega\mu_0 - \frac{\kappa^2}{\omega\varepsilon_0\varepsilon_d} \\ 0 & 0 & -\omega\mu_0 & 0 \\ 0 & -\omega\varepsilon_0\varepsilon_d + \frac{\kappa^2}{\omega\mu_0} & 0 & 0 \\ \omega\varepsilon_0\varepsilon_d & 0 & 0 & 0 \end{bmatrix}.$$

The longitudinal components of electric and magnetic field phasors in term of transverse components are

$$e_z(z) = -\frac{\kappa}{\omega\varepsilon_0\varepsilon_r(z)} h_y(z)\,, \tag{2}$$

$$h_z(z) = \frac{\kappa}{\omega\mu_0} e_y(z)\,. \tag{3}$$

To characterize the optical response of one period of the PMLID materials, the solution of (1) in half-spaces ($z \gtrless d^{\pm}$) may be written as [28, 29]

$$[\mathbf{f}(\pm\Lambda^{\pm})] = [\underline{\underline{R}}^{\pm}] \cdot [\mathbf{f}(d^{\pm})]\,, \tag{4}$$

where

$$[\underline{\underline{R}}^{\pm}] = \exp\{i[\underline{\underline{G}}_9^{\pm}](\pm d)\} \cdot \exp\{i[\underline{\underline{G}}_8^{\pm}](\pm d)\} \cdots \exp\{i[\underline{\underline{G}}_1^{\pm}](\pm d)\}\,.$$

With the help of Bloch (Floquet-Lyapunov) theorem [29], matrices $[\underline{\underline{R}}^{\pm}]$ can be expressed as

$$[\underline{\underline{R}}^{\pm}] = \exp\{\pm i\Lambda^{\pm}[\tilde{\underline{\underline{R}}}^{\pm}]\}\,, \tag{5}$$

where $[\tilde{\underline{\underline{R}}}^{\pm}]$ are dummy matrices. Matrices $[\underline{\underline{R}}^{\pm}]$ and $[\tilde{\underline{\underline{R}}}^{\pm}]$ share the same eigenvectors and their eigenvalues are also related [30]. Let $[\mathbf{v}_n^{\pm}]$, $(n \in [1,4])$, be the eigenvectors of $[\underline{\underline{R}}^{\pm}]$ corresponding to its nth eigenvalue $q_n^{\pm}$; then, the corresponding eigenvalues $\tilde{q}_n^{\pm}$ of $[\tilde{\underline{\underline{R}}}^{\pm}]$ are related by the following identity

$$\tilde{q}_n^{\pm} = \mp i\frac{\ln q_n^{\pm}}{\Lambda^{\pm}}. \tag{6}$$

By ensuring $\mathrm{Im}[\tilde{q}_{1,2}^{\pm}] \gtrless 0$, the fields' magnitudes in (4) at the interfaces $z = d^{\pm}$ can be written as

$$[\mathbf{f}(d^{+})] = [[\mathbf{v}_1^{+}]\ \ [\mathbf{v}_2^{+}]] \cdot \begin{bmatrix} c_1 \\ c_2 \end{bmatrix}, \tag{7}$$

and

$$[\mathbf{f}(d^{-})] = [[\mathbf{v}_1^{-}]\ \ [\mathbf{v}_2^{-}]] \cdot \begin{bmatrix} a_1 \\ a_2 \end{bmatrix}. \tag{8}$$

The solution of (1) in the region ($d^{+} \le z \le d^{-}$) occupied by dielectric defect can be defined as

$$[\mathbf{f}(d^{+})] = \exp\{i[\underline{\underline{G}}^{D}](d^{+} - d^{-})\} \cdot [\mathbf{f}(d^{-})]\,. \tag{9}$$

Rearranging (7), (8), and (9) results in the following matrix equation

$$[\underline{\underline{W}}(\kappa)] \cdot \begin{bmatrix} a_1 \\ a_2 \\ c_1 \\ c_2 \end{bmatrix} = 0\,. \tag{10}$$

For non-trivial solution of (10), the 4×4 matrix $[\underline{\underline{W}}(\kappa)]$ must be singluar. Therefore,

$$\det[\underline{\underline{W}}(\kappa)] = 0\,, \tag{11}$$

is the dispersion relation of Tamm wave with Uller-Zenneck wave characteristic for both p- and s-polarization states.

3. Numerical Results and Discussion

A computer program was prepared to calculate the numerical solution of (11), for relative wavenumber $\kappa/k_\circ$ of the excited Tamm wave, by incorporating search and Newton-Raphson methods [28]. All the numerical results were obtained at fixed free space wavelength $\lambda_0 = 633$nm and varying dielectric defect thickness $L_s \in [0, 300\text{nm}]$. The dielectric defect is characterized by relative permittivity $\varepsilon_d = 14.461 + i1.1936$, which is a non-plasmonic analog of silver with skin depth $\Delta_d = 1/\text{Im}[k_\circ\sqrt{\varepsilon_d}] \approx 642$nm [25]. It is worth mentioning here that the solutions for the three different boundary value problems shown in Fig. 1 are evaluated for $L_s < \Delta_d$ at which the two interfaces of dissipative dielectric defect are assumed to be strongly coupled and guide compound Tamm waves [25, 31]. The solutions for the three cases are also evaluated for $L_s = 2\Delta_d$, which represent decoupling of dissipative dielectric defect interfaces that guide Tamm waves at either or both interfaces individually.

Before detail numerical discussion, let us elucidate that what parameters should we consider to discriminate loosely and strongly bounded Tamm waves at the two interfaces of dissipative dielectric defect and how to separate Tamm waves from waveguide modes in the proposed canonical boundary value problems. This discussion is followed in the proceeding paragraphs.

Let consider that $L_s \to 0$, then, the proposed problem reduce to PMLID/PMLID configuration. In order to quantify the loosely and strongly bounded Tamm waves at interface $z = 0$, let define $\beta^+_{1,2} = \text{Im}[\tilde{q}^+_{1,2}] \cdot \Lambda^+$ and $\beta^-_{1,2} = -\text{Im}[\tilde{q}^-_{1,2}] \cdot \Lambda^-$ in the two half-spaces $z > 0$ and $z < 0$, respectively. For the Tamm waves on both sides of the interface, the four decay constants $\exp\{-\beta^+_{1,2}\}$ and $\exp\{-\beta^-_{1,2}\}$ must have values less than unity to decay exponentially as $z \to \pm\infty$. Therefore, the Tamm wave is strongly bounded to the interface when the decay constant is closed to zero and the Tamm wave is loosely bounded to the interface when the decay constant is closed to unity, [32].

Let now consider that $L_s \neq 0$, which results in PMLID/dissipative-dielectric/PMLID configuration as shown in Fig. 1. In this configuration the strongly and loosely bounded Tamm waves towards the right and left of interface planes $z = d^+$ and $z = d^-$, respectively, still depend on the decay constants; because the half-spaces are occupied by infinite PMLID materials. However, the strongly and loosely bounded Tamm waves towards the left and right of interface planes $z = d^+$ and $z = d^-$, respectively, inside the interposed dielectric defect depend on the skin depth Δ_d versus dielectric defect thickness L_s. For $L_s < \Delta_d$ indicate strongly/loosely bounded Tamm waves depending upon the values of $\text{Re}[\kappa/k_\circ]$ and the two interfaces are virtually coupled. When $L_s > \Delta_d$ then, the two interfaces virtually become decoupled and support either loosely bounded Tamm wave to both or single interfaces of dielectric defect or waveguide modes, [25, 33].

As the interposed material is dissipative in the presented problem, which result in complex wavenumber in the direction of wave propagation (x-axis). Therefore, the strongly and loosely bounded Tamm waves to one or two interfaces of dissipative dielectric defect can also be quantified with help of propagation distance $\Delta_{prop} = 1/\text{Im}[\kappa]$. Δ_{prop} is the distance in the direction of wave propagation at which the amplitude of the wave decreases by a factor of $\exp(-1) \approx 0.367$ and the power density decreases by a factor $\exp(-2) \approx 0.135$. Hence, the relative values of Δ_{prop} at any dielectric defect thickness indicate that the small value of Δ_{prop} represent strongly bounded Tamm wave to either or both interfaces of dissipative dielectric defect and

the large value of Δ_{prop} represent loosely bounded Tamm wave to either or both interfaces of dissipative dielectric defect, [25].

Keeping in mind the aforementioned discussion, the discrimination between Tamm waves and waveguide modes propagation in lossy dielectric materials can be accomplished with the help of time-average power density which is defined as $\mathbf{P}(z) = \frac{1}{2}\mathrm{Re}\{\mathbf{E}(z) \times \mathbf{H}^*(z)\}$, where "*" denote conjugate of magnetic field. The power density profile represent Tamm wave when large fraction of energy reside in half-spaces occupied by PMLIDs having maximum power density either at the interfaces of dissipative dielectric (representing strongly bounded Tamm waves) or in the partnering PMLIDs (representing loosely bounded Tamm waves). The power density profile represent waveguide mode when maximum power density is guided by the dissipative dielectric defect as compared to rapidly diminishing energy in partnering PMLIDs.

It is to be noted that the phase speed of Tamm wave is given by $v_{ph} = \omega/\mathrm{Re}[\kappa]$ or $v_{ph} = c_\circ/\mathrm{Re}[\kappa/k_\circ]$, where $c_\circ$ is speed of light. Therefore, the Tamm wave is high phase speed wave when $v_{ph}/c_\circ > 1$ and the Tamm wave is low phase speed wave when $v_{ph}/c_\circ < 1$.

The numerical results of each of the three cases shown in Fig. 1 are now presented in the following subsections.

3.1. Case-I

Let consider the boundary value problem shown in Fig. 1(a). Fig. 2(a) represents multiple solutions of the dispersion relation (11) of Fig. 1(a), for $\mathrm{Re}[\kappa/k_\circ]$ vs. L_s. In the figure, $(p_1 - p_6)$ branches represent p-polarized wave solutions and $(s_1 - s_6)$ branches represent s-polarized wave solutions. It is to be noted that all solution branches of s-polarized wave represent waveguide modes while p-polarized wave solutions represent either Tamm waves or waveguide modes. The figure is divided into unshaded and gray shaded regions on the basis of threshold value $\kappa_{th1} = \mathrm{Re}[\kappa/k_\circ] \approx 2.3$. The unshaded region comprises the solution branches of p-polarized Tamm waves and s-polarized waveguide modes whereas the gray shaded region comprises of the solution branches of waveguide modes of both linear polarization states. In other words, κ_{th1} distinguishes p-polarized Tamm waves (solutions in unshaded region) from p-polarized waveguide modes (solutions in gray shaded region). The value of κ_{th1} was found for all branches of Fig. 2(a), on the basis of thorough analysis of data given in Fig. 2(a) with the help of power density profiles. It was also found that κ_{th1} is independent of the dissipative dielectric defect thickness i.e. for any L_s value it differentiate Tamm wave and waveguide mode. Multiple solutions appeared for $L_s \geq 2$nm whereas at least three possible solutions exist at $L_s = 0$; one represent p-polarized Tamm wave [34] with non-Uller-Zenneck wave characteristic and the other two represent s-polarized waveguide modes. These solutions are not clearly identifiable from Fig. 2(a) because of high proximity of solutions at $L_s = 0$ and $L_s = 2$nm. Therefore, a separate subplot of Fig. 2(a) is provided in Fig. 3 to give a clear picture of the solutions at $L_s = 0$ and $L_s = 2$nm. The solution branches in Fig. 2(a) of both polarization states are increasing with increasing values of L_s. The maximum value of $\mathrm{Re}[\kappa/k_\circ] \approx 3.705$ on branch s_6 was found for $L_s \leq 300$nm. It is clear from the figure that the corresponding phase speed of both polarization states are varying in descending fashion. No high phase speed solution branch of p-polarization state was found except a single branch (s_1) of s-polarization state that occur at $\mathrm{Re}[\kappa/k_\circ] < 1.0$ represent high phase speed solutions. The plot of Δ_{prop} vs. L_s is shown in Fig. 2(b). The figure represents the corresponding

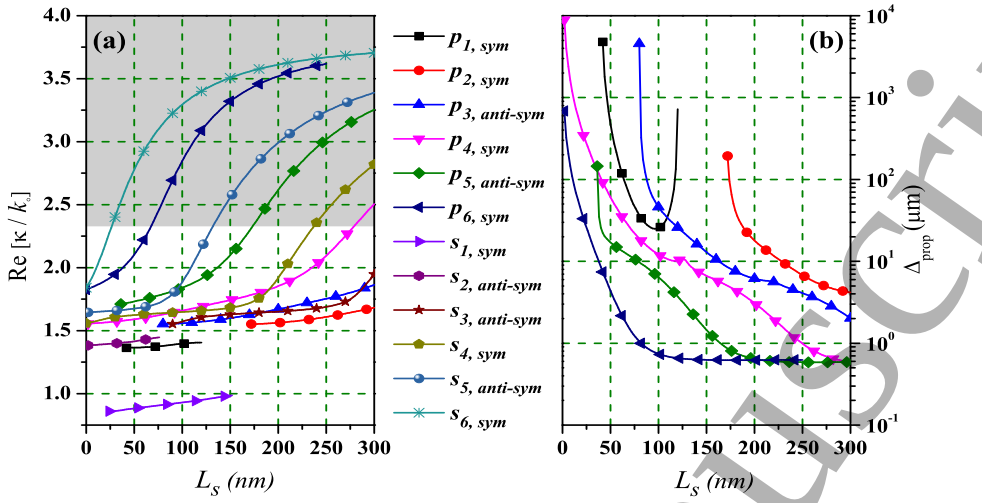

Figure 2. (a) The real part of the complex relative wavenumber $\kappa/k_\circ$ of excited Tamm waves and waveguide modes as a function of varying thickness of dielectric defect $L_s \in [0, 300\text{nm}]$ for the case shown in Fig. 1(a). The relative permittivities of PMLID are given in Table 1, at free space wavelength $\lambda_\circ = 633\text{nm}$, with a period $\Lambda^{\pm} = 675\text{nm}$ consisting of nine different layers of silicon-oxynitrides each of thickness $d = 75\text{nm}$. The relative permittivity of dissipative dielectric defect is $\varepsilon_d = 14.461 + i1.1936$. Shaded region represent waveguide modes' solutions and unshaded region represents p-polarized Tamm waves and s-polarized waveguide modes. "sym" and "anti-sym" denote symmetric and ant-symmetric solution branches. (b) Represents variation in Δ_{prop}, for branches $(p_1 - p_6)$ of Fig. 2(a), as a function of increasing thickness L_s of dissipative dielectric defect.

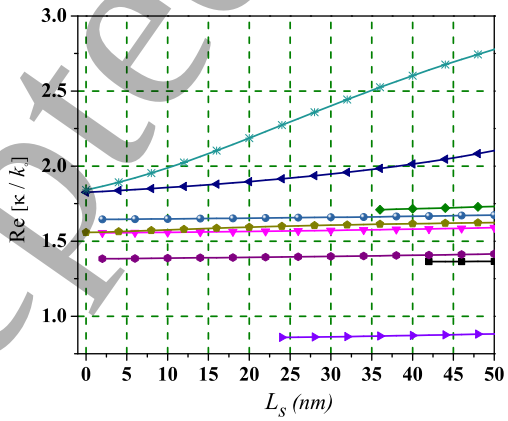

Figure 3. Subplot of Fig. 2(a) for $L_s \in [0, 50\text{nm}]$. Branches (p_4, s_2, and s_5) begin at $L_s = 2\text{nm}$ and branches (p_6, s_4, and s_6) begin at $L_s = 0$ in Fig. 2(a).

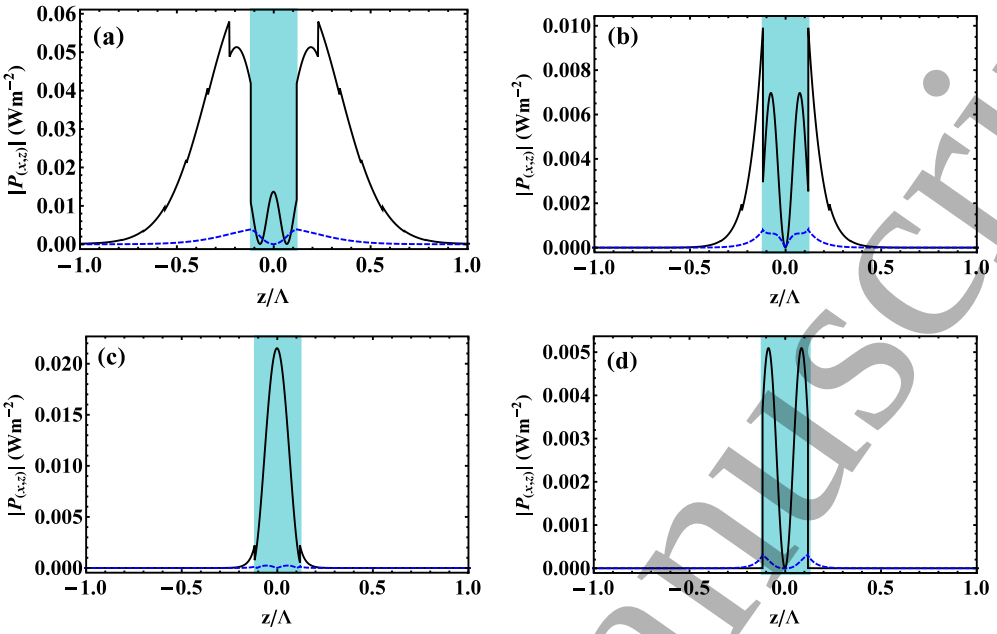

Figure 4. Profiles of $\hat{u}_x$(black solid line) and $\hat{u}_z$(blue dashed line) components of the time average power density of Tamm waves and waveguide modes along z-direction, calculated using $a_1 = a_2 = 1\text{Vm}^{-1}$. All other parameters are the same as in Fig. 2(a). These plots are obtained for dissipative dielectric defect (light blue shaded region) having thickness $L_s = 160\text{nm}$ and (a) $\kappa/k_\circ = 1.7603 + i0.0171$ on branch p_4; (b) $\kappa/k_\circ = 2.1891 + i0.0909$ on branch p_5; (c) $\kappa/k_\circ = 3.3734 + i0.1617$ on branch p_6; (d) $\kappa/k_\circ = 2.6653 + i0.1606$ on branch s_5.

Δ_{prop} of p-polarization state solution branches shown in Fig. 2(a). In Fig. 2(b), the p-polarization state Δ_{prop} branches are organized in reverse order to that shown in Fig. 2(a), i.e. the lowest (bottom) branch in Fig. 2(b) represent the Δ_{prop} of p_6 (top) branch in Fig. 2(a) and the top branch (black colored) in Fig. 2(b) represent the Δ_{prop} of p_1 branch (bottom black colored) in Fig. 2(a). A similar discussion can be made for the rest of the branches in the two figures. This mean that the large values of $\text{Re}[\kappa/k_\circ]$ in Fig. 2(a) correspond to small values of Δ_{prop} in Fig. 2(b) and vice versa. Therefore, the large values of Δ_{prop} represent relatively high phase speed p-polarized Tamm waves and the small values of Δ_{prop} represent relaively low phase speed p-polarized Tamm waves or waveguide modes. However, it is evaluated that none of the p-polarization state solution's phase speed exceed the speed of light $c_\circ$. Hence, the results are in close agreement with the results presented in (Sec. B, [25]). It is clear from Fig. 2(b) that each branch of Δ_{prop} decreases with increasing values of L_s. However, beyond at some specific value of L_s the branches becomes steady with increasing values of L_s, which represent waveguide modes. For instance, in Fig. 2(b) for $L_s \geq 160\text{nm}$ on branch p_6 the values of Δ_{prop} are in steady form with increasing values of L_s. It is concluded that each branch of Δ_{prop} has uniform values beyond at some specific value of L_s, except branch p_1 which first decreases and then increase with increasing L_s about $L_s \approx 100\text{nm}$. Thus, any branch of Δ_{prop} below some specific

Table 2. The p-polarization state solutions of dispersion relation (11) of Fig. 1(a), for $\kappa/k_\circ$ at $L_s = 2\Delta_d = 1284$nm.

	p_1	p_2	p_3	p_4	p_5	p_6	p_7	p_8
Re$[\kappa/k_\circ]$	0.8975	1.6285	1.8993	2.2005	2.4837	2.7289	2.9396	3.6798
Im$[\kappa/k_\circ]$	0.1956	0.0875	0.1766	0.2249	0.2194	0.2073	0.1961	0.1617

value of L_s represent Tamm waves and beyond it represent waveguide modes.

The representative spatial profiles of x- and z-components of the time-average power density are shown in Fig. 4 for both polarization states, which consists of four subplots. Fig. 4(a), (b), (c), and (d) are respectively plotted at $L_s = 160$nm with $\kappa/k_\circ = 1.7603 + i0.0171$ on branch p_4; $\kappa/k_\circ = 2.1891 + i0.0909$ on branch p_5; $\kappa/k_\circ = 3.3734 + i0.1617$ on branch p_6; and $\kappa/k_\circ = 2.6653 + i0.1606$ on branch s_5. For p-polarized solution branches, the loosely and strongly bounded Tamm waves were differentiated at threshold $\kappa_{th2} = \text{Re}[\kappa/k_0] \approx 1.82$. The value of κ_{th2} was also found for all p-polarized branches of Fig. 2(a) by thoroughly noticing the transformation of power density profiles from loosely bounded to tightly bounded Tamm waves. Therefore, plot of Fig. 4(a) obtained at $\text{Re}[\kappa/k_\circ] = 1.76 < \kappa_{th2}$ represent loosely bounded Tamm wave having decay constant 0.0433 at PMLID side of interfaces and $\Delta_{prop} = 5.9\mu$m in direction of wave propagation. Fig. 4(b) obtained at $\text{Re}[\kappa/k_\circ] = 2.19 > \kappa_{th2}$ represent strongly bounded Tamm wave with decay constant 8.2×10^{-5} at PMLID side of interfaces and $\Delta_{prop} = 1.1\mu$m. Hence, loosely bounded Tamm waves' Δ_{prop} is larger than that of strongly bounded Tamm waves. Similarly, loosely bounded Tamm waves' phase speed is relatively higher than that of tightly bounded Tamm waves. Fig. 4(c) represent p-polarized waveguide mode because most of the power is guided by the dissipative defect. The plot is obtained at $\text{Re}[\kappa/k_\circ] = 3.73$ that lies in shaded region of Fig. 2(a) with propagation distance $\Delta_{prop} = 0.62\mu$m. Fig. 4(d) is a representative power density plot of s-polarized waveguide mode. Let us note that the local maxima of P_x in Fig. 4(a) and (c) occur inside the dielectric defect at $z = 0$, represent symmetric solutions. In Fig. 4(b) and (d) the local minima of P_x inside the dielectric defect occur at $z = 0$, hence, represent anti-symmetric solutions [31]. Therefore, on the basis of local maxima and minima of P_x at $z = 0$ inside the dielectric defect, the solution branches of both polarization states shown in Fig. 2 are classified into symmetric and anti-symmetric solutions, respectively. The classification of symmetric and anti-symmetric solution branches in Fig. 2(a) rely on P_x because of its dominant behavior over P_z.

In order to verify if the thresholds κ_{th1} and κ_{th2} hold for $L_s > \Delta_d$, the p-polarized solutions at $L_s = 2\Delta_d = 1284$nm are given in Table 2. Representative power density profile for solution p_2 and p_5 of Table 2 are shown in Fig. 5(a) and (b), respectively. Fig. 5(a) represent loosely bounded Tamm wave since it is obtained at $\text{Re}[\kappa/k_\circ] = 1.63 < \kappa_{th2}$ whereas Fig. 5(b) represent waveguide mode because $\text{Re}[\kappa/k_\circ] = 2.48 > \kappa_{th1}$. This brings us to conclude that the thresholds are even held for larger values of L_s. Besides, the two interfaces of dielectric defect are decoupled but still guide equal magnitude's Tamm waves and waveguide modes. The power density profiles shown in Fig. 5 represent anti-symmetric solutions.

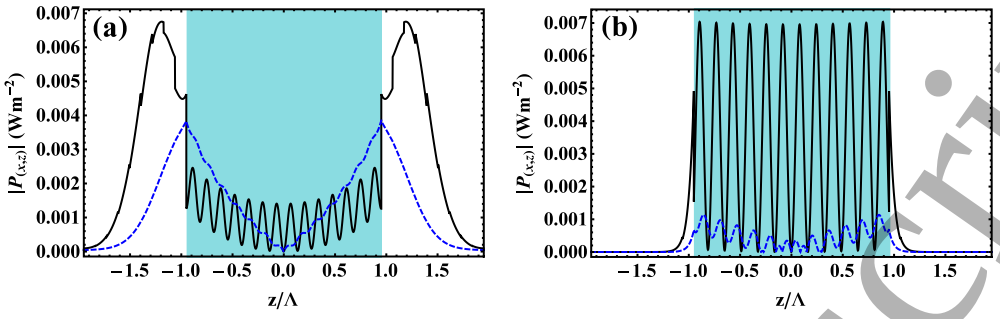

Figure 5. Black solid line represent $\hat{u}_x$ and blue dashed line represent $\hat{u}_z$ components of time average power density as a function of z-axis, of p-polarization state, at $L_s = 1284$nm (light blue shaded region) for *Case-I* having (a) $\kappa/k_\circ = 1.6285 + i0.0875$ (p_2 of Table 2); (b) $\kappa/k_\circ = 2.4837 + i0.2194$ (p_5 of Table 2). Other p-polarized solutions at $L_s = 1284$nm are listed in Table 2.

3.2. Case-II

The schematic diagram of the canonical boundary value problem shown in Fig. 1(b) is evaluated for multiple Tamm waves having Uller-Zenneck wave characteristics. The solutions of the dispersion relation (11) of this case as a function of varying L_s are shown in Fig. 6(a). The solution branches in Fig. 6(a) are organized into six branches of p-polarization states and five branches of s-polarization states and marked as $(p_1 - p_6)$ and $(s_1 - s_5)$, respectively. It is observed that the threshold ($\kappa_{th1} \approx 2.3$) of relative wavenumbers shown in Fig. 6(a) remains the same as that in *Case-I*, found with the help of power density profiles. Therefore, Fig. 6(a) is divided into gray shaded and unshaded regions on the basis of κ_{th1}.The gray shaded region consists of solution branches, having $\mathrm{Re}[\kappa/k_\circ] \geq \kappa_{th1}$, representing waveguide modes of both linear polarization states. The unshaded region comprises solution branches of p-polarized Tamm waves and s-polarized waveguide modes with $\mathrm{Re}[\kappa/k_\circ] < \kappa_{th1}$. Moreover, all the s-polarized solution branches represent waveguide modes. Solutions in Fig. 6(a) appear for L_s as small as 2nm which are not clearly visible. Therefore, a separate subplot of Fig. 6(a) is provided in Fig. 7 to avoid confusion with no solutions at $L_s = 0$. It was noticed that the maximum value of $\mathrm{Re}[\kappa/k_\circ]$ on branch s_5 in this case is the same as was found in *Case-I* for $L_s \leq 300$nm on branch s_6.

In Fig. 6(a), branch (p_1) of p-polarization state in the range $L_s \in [0, 90\text{nm}]$ denote high phase speed solutions that exceed the speed of light owing to $\mathrm{Re}[\kappa/k_\circ] < 1$. From the figure, it is clear that the phase speed of solution branches $(p_2 - p_6)$ and $(s_1 - s_5)$ decreases with increasing L_s, but none of them have phase speed higher than the speed of light.

The Δ_{prop} vs. L_s shown in Fig. 6(b) was calculated for p-polarized solution branches of Fig. 6(a). The Δ_{prop} of branches p_1 and p_2 in Fig. 6(b) first decrease and then increase in U-shape in the range $L_s < 90$nm. For branches $(p_3 - p_6)$, large values of Δ_{prop} correspond to relatively high phase speed waves and vice versa. In other words, small values of $\mathrm{Re}[\kappa/k_\circ]$ represent waves with large Δ_{prop} and large values of $\mathrm{Re}[\kappa/k_\circ]$ represent waves with relatively small Δ_{prop}. The Δ_{prop} curves undergo very little change for solutions representing waveguide modes.

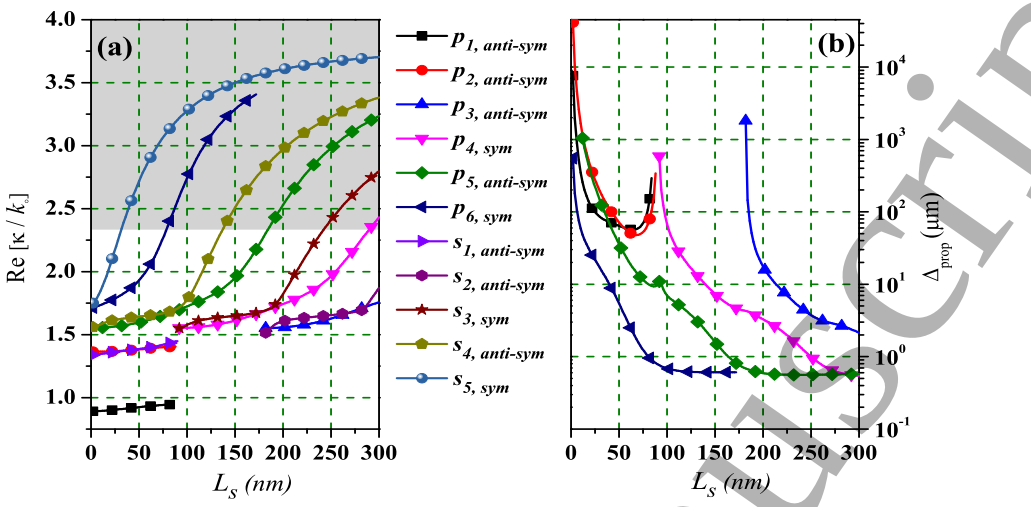

Figure 6. (a) Re$[\kappa/k_\circ]$ of excited Tamm waves and waveguide modes as a function of varying thickness of dielectric defect $L_s \in [0, 300\text{nm}]$ for the case shown in Fig. 1(b). All other parameters are the same as in Fig. 2. (b) Δ_{prop} as a function of dissipative defect thickness L_s, for branches $(p_1 - p_6)$ in part (a).

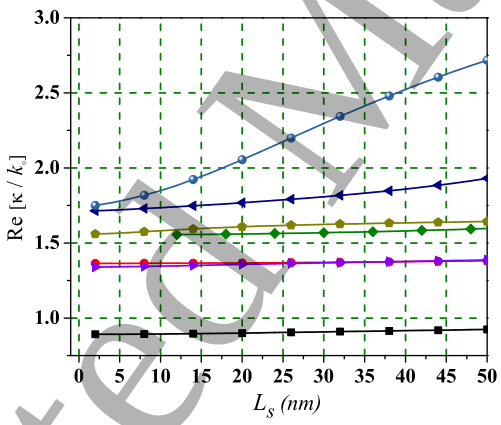

Figure 7. Subplot of Fig. 6(a) in the range $L_s \in [0, 50\text{nm}]$. Starting values of branches (p_1, p_2, p_6, s_1, s_4, and s_5) at $L_s = 2\text{nm}$ in Fig. 6(a).

The spatial profiles of power density's x- and z-components at fixed values of L_s and $\kappa/k_\circ$ are shown in Fig. 8. The power density distribution as a function of z-axis is shown in Fig. 8(a) at $L_s = 70\text{nm}$ with $\kappa/k_\circ = 1.6393 + i0.0075$ on branch p_5. The profile represent Tamm wave that is loosely bounded to the interface at $z = d^-$ having decay constant 0.205 at PMLID side of interfaces and $\Delta_{prop} = 13.5\mu\text{m}$. Contrary to this, the Tamm wave seems to be strongly bounded at interface $z = d^+$ in Fig. 8(a). This may be due to PMLID layer ($j = 9$) closest to the dielectric defect interface $z = d^+$. Fig. 8(b) plotted at $L_s = 70\text{nm}$ with $\kappa/k_\circ = 2.1786 + i0.0638$

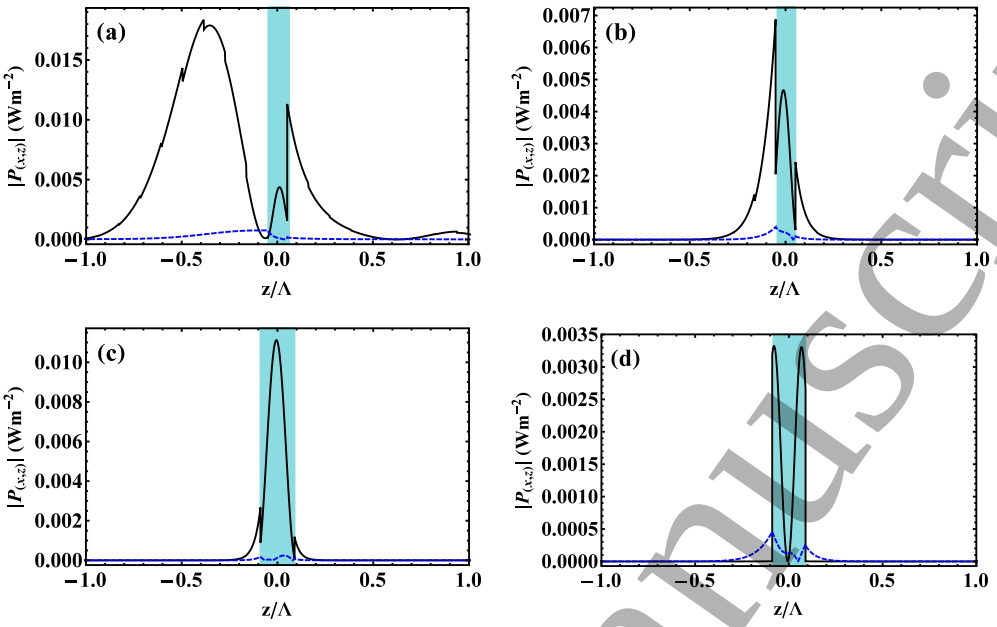

Figure 8. Profiles of $\hat{u}_x$(black solid line) and $\hat{u}_z$(blue dashed line) components of time average power density of Tamm waves and waveguide modes along z-direction obtained using $a_1 = a_2 = 1\text{Vm}^{-1}$. All other parameters are the same as in Fig. 6(a). The power density profile are obtained at dissipative dielectric defect (light blue shaded region) thickness $L_s = 70$nm with (a) $\kappa/k_\circ = 1.6393 + i0.0075$ on branch p_5; (b) $\kappa/k_\circ = 2.1786 + i0.0638$ on branch p_6, and $L_s = 120$nm with (c) $\kappa/k_\circ = 3.0261 + i0.1617$ on branch p_6; (d) $\kappa/k_\circ = 2.0674 + i0.1318$ on branch s_4.

on branch p_6, represent strongly bounded Tamm wave to the interfaces at $z = d^{\pm}$ with decay constant 9.3×10^{-5} at PMLID side of interfaces and $\Delta_{prop} = 1.58\mu$m. In Fig. 8(a) and (b), large fraction of energy resides in region $z < d^-$ as compared to small fraction of energy in region $z > d^+$ occupied by PMLIDs. The figures show unequal energy distribution in the two half-spaces. This may be due to asymmetric arrangement of PMLIDs' permittivities about the dielectric defect. It is apparent that loosely bounded Tamm waves have large values of Δ_{prop} and strongly bounded Tamm waves have small values of Δ_{prop}. The p- and s-polarized waveguide modes of Fig. 8(c) and (d), respectively, were obtained for $L_s = 120$nm with $\kappa/k_\circ = 3.0261 + i0.1617$ on branch p_6 and $\kappa/k_\circ = 2.0674 + i0.1318$ on branch s_4. Fig. 6, enlists the symmetric and anti-symmetric solution branches. It can be observed that anti-symmetric solution branches outnumbered the symmetric solution branches due to asymmetry in the permittivites of PMLIDs in the two half-spaces of Fig. 1(b).

The interfaces of dielectric defect (at $L_s < \Delta_d$) are assumed to be coupled for solutions of Tamm waves in unshaded region of Fig. 6(a). To justify this statement for large values of L_s, the dispersion relation solutions at $L_s = 2\Delta_d = 1284$nm resulted in eight p-polarized waves having relative wavenumbers given in Table 3. The power density profile of Fig. 9(a) obtained for solution p_2 of Table 3 depicts decoupling of intefaces having most energy of Tamm wave propagation in the vicinity

Table 3. The p-polarization state solutions of dispersion relation (11) of canonical problem shown in Fig. 1(b), at $L_s = 2\Delta_d = 1284$nm.

	p_1	p_2	p_3	p_4	p_5	p_6	p_7	p_8
$\mathrm{Re}[\kappa/k_\circ]$	0.9612	1.6744	1.8236	2.1667	2.4635	2.7158	2.9307	3.6789
$\mathrm{Im}[\kappa/k_\circ]$	0.2643	0.1289	0.1966	0.2399	0.2267	0.2113	0.1985	0.1619

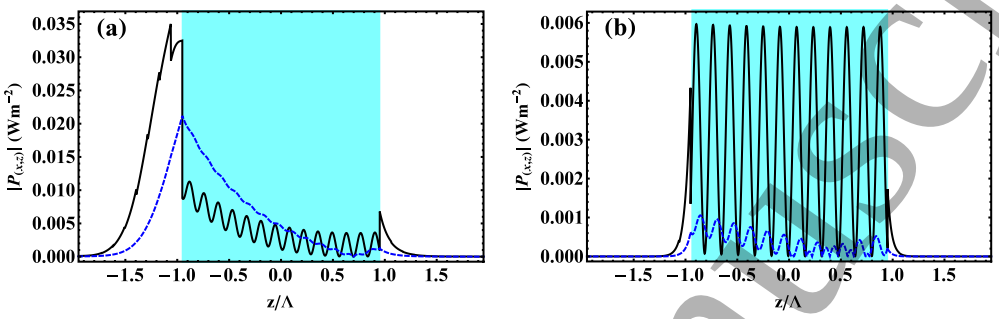

Figure 9. Representative spatial distribution of $\hat{u}_x$ (black solid line) and $\hat{u}_z$(blue dashed line) components of time average power density for data given in Table 3 at $L_s = 1284$nm (light blue shaded region) having (a) $\kappa/k_\circ = 1.6744 + i0.1289$ (p_2) and (b) $\kappa/k_\circ = 2.4635 + i0.2267$ (p_5).

of $z = d^-$ interface. This Tamm wave is loosely bounded to interface $z = d^-$ because $\mathrm{Re}[\kappa/k_\circ] = 1.67 < \kappa_{th2} \approx 1.82$, the value of threshold being found with the help of power density profiles obtained using the results of Fig. 6(a). Fig. 9(b), represent waveguide mode for solution p_5 in Table 3 obatined at $\mathrm{Re}[\kappa/k_\circ] = 2.46 > \kappa_{th1}$. Hence, the defined thresholds hold for large values of L_s but the increase in thickness of dissipative dielectric defect results in decoupling of interfaces for this case.

3.3. Case-III:

The dispersion relation (11) is solved for canonical BVP shown in Fig. 1(c) and the obtained solutions are presented in Fig. 10(a). In the figure, solution branches $(p_1 - p_4)$ and $(s_1 - s_5)$, respectively, represent p- and s-polarized waves. It is observed that all s-polarized branches represent waveguide modes. In Fig. 10(a), branches p_1 and s_1 represent high phase speed solutions because of $\mathrm{Re}[\kappa/k_\circ] < 1$ whereas all other branches represent solutions of low phase speed waves. Fig. 10(a), is divided into gray shaded and unshaded regions based on new threshold $\kappa_{th3} = \mathrm{Re}[\kappa/k_0] \approx 1.91$. This new threshold κ_{th3} was identified by analyzing the transformation of power density profile of Tamm wave into waveguide mode, found for all p-polarized branches of Fig. 10(a). This might also be due to the fact that the lowest refractive index of PMLID layers ($j = 9$) closest to the two interfaces of dissipative dielectric defect. Hence, the portion of branches p_3 and p_4 in shaded region of Fig. 10(a) represent solutions of waveguide modes. The unshaded region comprises of solutions of p-polarized Tamm waves and s-polarized waveguide modes. Fig. 11, provide subplot of Fig. 10(a) in the range $L_s \in [0, 50\mathrm{nm}]$ to clarify the starting values of two solution branches p_2 and s_5 at $L_s \approx 2$nm and no solution at $L_s = 0$. It was observed that the maximum value of $\mathrm{Re}[\kappa/k_\circ] \approx 3.69$ was attained for $L_s \leq 300$nm on branch p_4 and s_5. Let us note

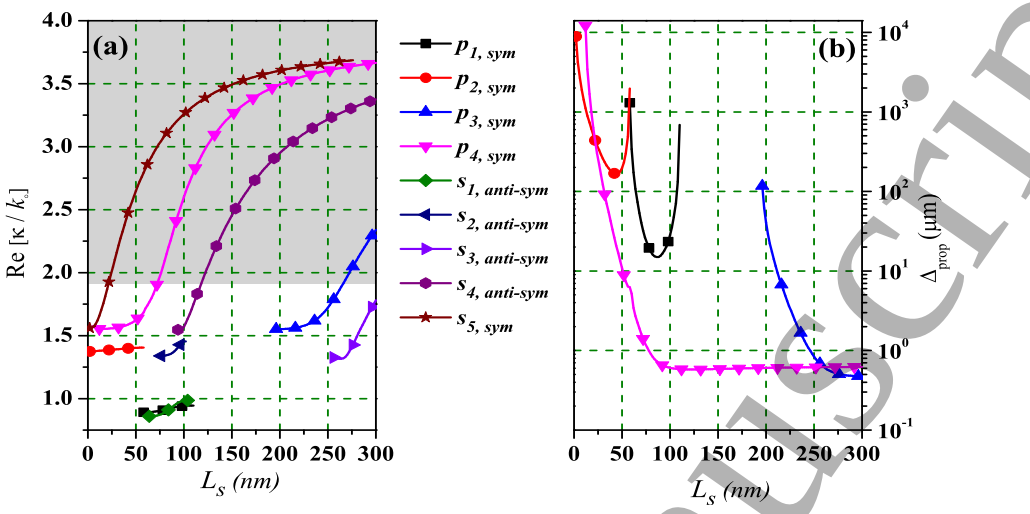

Figure 10. (a) Re$[\kappa/k_\circ]$ of excited Tamm waves and waveguide modes as a function of varying thickness of dielectric defect $L_s \in [0, 300\text{nm}]$ for the case shown in Fig. 1(c). All other parameters are the same as in Fig. 2. (b) Corresponding Δ_{prop} values computed for branches $(p_1 - p_4)$ in part(a) as a function of L_s.

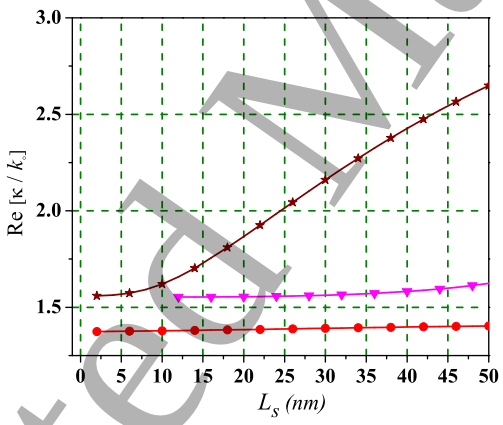

Figure 11. Subplot of Fig. 10(a) in the range $L_s \in [0, 50\text{nm}]$. Starting values of branches p_2 and s_5 at $L_s = 2\text{nm}$ in Fig. 10(a).

that all solution branches of p-polarization state represent symmetric solutions and except, one symmetric solution branch (s_5), the remaining four solution branches of s-polarization state represent anti-symmetric solutions.

The Δ_{prop} for p-polarized branches of Fig. 10(a) are plotted as function of L_s in Fig. 10(b). It is to be noted that the Δ_{prop} values of p-polarized Tamm waves are larger than the Δ_{prop} values of waveguide modes. Moreover, the propagation distance of waveguide modes undergo little change with increasing L_s values. It can also be observed from the figure that a decrease in propagation distance with increasing L_s

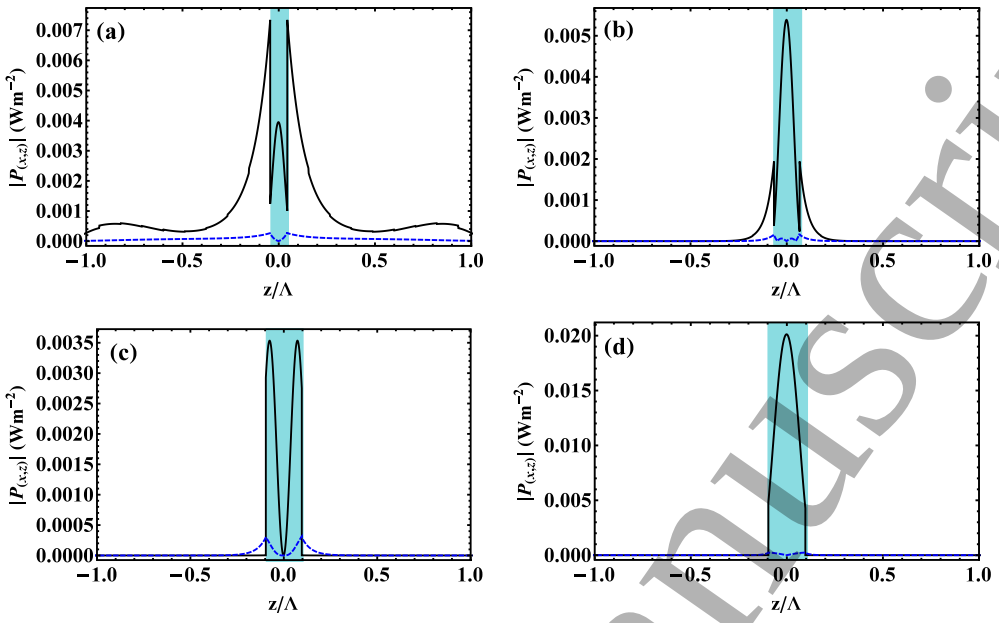

Figure 12. Spatial profiles of $\hat{u}_x$(black solid line) and $\hat{u}_z$(blue dashed line) components of time average power density of Tamm waves and waveguide modes as a function of z-axis, considering $a_1 = a_2 = 1\text{Vm}^{-1}$. All other parameters are the same as in Fig. 10(a). The dissipative dielectric defect is represented by light blue shaded region with thickness (a) $L_s = 60$nm having $\kappa/k_\circ = 1.7158 + i0.0195$ on branch p_4; (b) $L_s = 90$nm having $\kappa/k_\circ = 2.3596 + i0.1489$ on branch p_4; (c) $L_s = 130$nm having $\kappa/k_\circ = 2.1406 + i0.1663$ on branch s_4; (d) $L_s = 130$nm having $\kappa/k_\circ = 3.4213 + i0.1613$ on branch s_5.

Table 4. The p-polarization state solutions of dispersion relation (11) of canonical problem shown in Fig. 1(c), at $L_s = 2\Delta_d = 1284$nm.

	p_1	p_2	p_3	p_4	p_5	p_6	p_7	p_8
Re$[\kappa/k_\circ]$	1.0075	1.3688	1.7465	2.1309	2.4424	2.7022	2.9215	3.5120
Im$[\kappa/k_\circ]$	0.3212	0.0438	0.2788	0.2603	0.2351	0.2157	0.2011	0.1693

reveal a decrease in phase speed of Tamm wave.

The representative spatial distribution of power density of Tamm wave for Re$[\kappa/k_\circ] = 1.72 < \kappa_{th3}$ is shown in Fig. 12(a) at $L_s = 60$nm with $\kappa/k_\circ = 1.7158 + i0.0195$ on branch p_4. The Tamm wave is strongly bounded to both interfaces of dielectric defect having decay constant 0.19 and propagation distance 5.18μm. Fig. 12(b) represent waveguide mode for Re$[\kappa/k_\circ] = 2.36 > \kappa_{th3}$ at $L_s = 90$nm with $\kappa/k_\circ = 2.3596 + i0.1489$ on branch p_4. This waveguide mode has relatively small propagation distance of 0.68μm as compared to Tamm waves. Fig. 12(c) and (d) at $L_s = 130$nm with $\kappa/k_\circ = 2.1406 + i0.1663$ on branch s_4 and $L_s = 130$nm with $\kappa/k_\circ = 3.4213 + i0.1613$ on branch s_5, respectively, represent s-polarized waveguide modes. With reference to Fig. 12, the solution branches shown in Fig. 10 are classified into symmetric and anti-symmetric solution branches.

To study the characteristics at much large values of L_s, the solution of dispersion

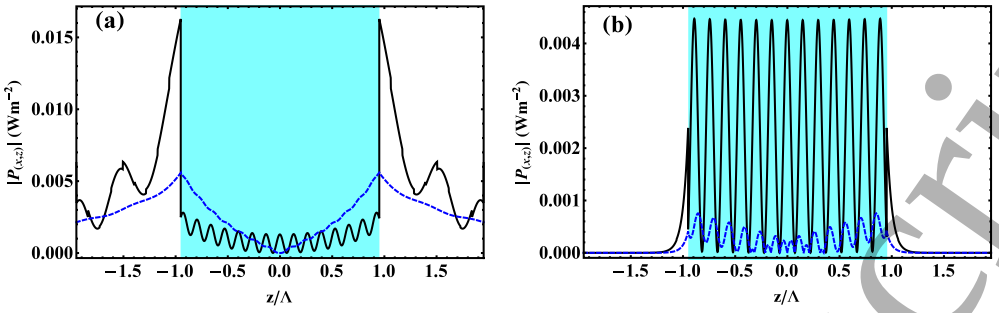

Figure 13. Power density profiles having $\hat{u}_x$ (black solid line) and $\hat{u}_z$ (blue dashed line) components obtained for canonical problem of Fig. 1(c) at $L_s = 1284$nm (Table 4). The relative wavenumbers are (a) $\kappa/k_\circ = 1.3688 + i0.0438$ (p_2) and (b) $\kappa/k_\circ = 2.1309 + i0.2603$ (p_4).

relation at thickness of dielectric defect two times its skin depth are given in Table. 4. Power density profiles for solution p_2 and p_4 of this table are shown in Fig. 13. These plots suggest that the threshold κ_{th3} is independent of L_s and the interfaces are also decoupled and each interface guide individual Tamm waves. In Fig. 13(a) and (b) the power density distributions represent symmetric solutions.

4. Concluding Remarks

The excitation of multiple compound Tamm waves with Uller Zenneck wave characteristics were theoretically investigated at the planar interfaces of dissipative dielectric defect sandwiched between two half spaces occupied by PMLID materials. The dispersion relation was numerically solved for three different configurations of the proposed problem for varying thickness of dissipative dielectric defect. In order to make sure the coupling in between two interfaces of dielectric defect, the varying thickness of dielectric defect was restricted to approximately lesser than half of the skin depth of dissipative dielectric defect. It was observed that the proposed structure support only p-polarized Tamm waves. All s-polarization state solutions resulted in waveguide modes. The loosely and strongly bounded Tamm waves at the interfaces of dielectric defect were discriminated using the concept of decay constant and propagation distance. However, the propagation distance is the best choice to discriminate the two types of Tamm waves. For loosely bounded Tamm waves the values of propagation distance are larger than the strongly bounded Tamm waves. Besides, in *Case-I* and *Case-II* same threshold value of real part of relative wavenumber (κ_{th2}) was found, which separate loosely bounded Tamm waves from strongly bounded Tamm waves. No such threshold value of real part of relative wavenumber was found in *Case-III*.

It was also noticed that the small values of propagation distance represented waveguide modes and the large values of propagation distance represented Tamm waves. However, in all three cases two different thresholds of real part of relative wavenumbers (κ_{th1} in *Case-I* and *Case-II* and κ_{th3} in *Case-III*) were quantified that discriminate Tamm waves from waveguide modes. The solutions of the three cases were also reported for a fixed value of dielectric defect thickness that was set equal to

double of skin depth of dissipative dielectric defect. At this value of dielectric defect thickness the two interfaces of defect decoupled and supported *p*-polarized Tamm waves to either or both interfaces of dielectric defect as well as waveguide modes of both polarization states. As the thresholds of real part of relative wavenumber were found to remain the same for any dielectric defect thickness, hence, produced no effect on the separation of Tamm waves from waveguide modes. No solution of Tamm wave and waveguide mode was found in the absence of dielectric defect, except in *Case-I* which resulted in one *p*-polarized Tamm wave and two *s*-polarized waveguide modes. At any value of dielectric defect thickness greater than or equal to 2nm, multiple compound Tamm waves and waveguide modes were found, which propagated with different phase speeds, different propagation distances, and different power density profiles at same frequency. It was observed that the multiplicity of guided Tamm waves having Uller-Zenneck characteristics alters upon using different arrangements of PMLID material permittivities. We hope that the study of compound Tamm waves may offer potential applications in multi-channel communication and muti-analyte sensors, etc.

5. Acknowledgment

We are highly thankful to the anonymous reviewers for their invaluable suggestions and corrections, which greatly improved the numerical representation of the work.

References

[1] Wood, R.W., "A suspected case of the electrical resonance of minute metal particles for light-waves. A new type of absorption," The London, Edinburgh, and Dublin Philosophical Magazine and Journal of Science, 3(16), pp.396-410 (1902).
[2] Fano, U., "The theory of anomalous diffraction gratings and of quasi-stationary waves on metallic surfaces (Sommerfeld's waves)," J. Opt. Soc. Am., 31(3), pp.213-222 (1941).
[3] Surface Plasmon Resonance Based Sensors, edited by J. Homola (Springer, Heidelberg, 2006).
[4] S. A. Maier, Plasmonics: Fundamentals and Applications (Springer, New York, 2007).
[5] Otto, A., "Excitation of nonradiative surface plasma waves in silver by the method of frustrated total reflection," Zeitschrift für Physik A Hadrons and nuclei, 216(4), pp.398-410 (1968).
[6] Kretschmann, E. and Raether, H.Z., Naturforsch, "Radiative Decay of Non Radiative Surface Plasmons Excited by Light," 2135, 2136, p.2135 (1968).
[7] Shinn, M. and Robertson, W.M., "Surface plasmon-like sensor based on surface electromagnetic waves in a photonic band-gap material," Sensors and Actuators B, 105(2), pp.360-364 (2005).
[8] Konopsky, V.N. and Alieva, E.V., "Photonic crystal surface waves for optical biosensors," Analytical Chemistry, 79(12), pp.4729-4735 (2007).
[9] J. A. Polo Jr. and A. Lakhtakia, "Surface electromagnetic waves: A review," Laser and Photonics reviews, 5, 234, (2011).
[10] Uller K., "Beiträge zur Theorie der elektromagnetischen Strahlung," Ph.D. thesis (Universität Rostock), Chap. XIV (1903).
[11] Zenneck J., "Über die Fortpflanzung ebener elektromagnetischer Wellen längs einer ebenen Lieterfläche und ihre Beziehung zur drahtlosen Telegraphie," Ann. Phys. Lpz. 23, 846–866 (1907).
[12] Sommerfeld A., "Über die Ausbreitung der Wellen in der drahtlosen Telegraphie," Ann. Phys. Lpz. 28, 665–736 (1909).
[13] Sommerfeld A., "Über die Ausbreitung der Wellen in der drahtlosen Telegraphie," Ann. Phys. Lpz. 81, 1135–1153 (1926).
[14] Faryad, M. and Lakhtakia, A., "Grating-coupled excitation of the Uller–Zenneck surface wave in the optical regime," JOSA B, 31(7), pp.1706-1711 (2014).
[15] Faryad, M. and Lakhtakia, A., "Observation of the Uller–Zenneck wave," Optics letters, 39(17), pp.5204-5207 (2014).

[16] Wait, J.R., *The ancient and modern history of EM ground-wave propagation,* IEEE Antennas and Propagation Magazine, 40(5), pp.7-24 (1998).
[17] Collin, R.E., *Field Theory of Guided Waves*, 2nd edn (New York: IEEE) (1991).
[18] Wait, J.R., "Electromagnetic Waves in Stratified Media: Revised Edition Including Supplemented Material," (Vol. 3), Elsevier (2013).
[19] Faryad, M. and Lakhtakia, A., "Grating-coupled excitation of the Uller–Zenneck surface wave in the optical regime," J. Opt. Soc. Am. B, 31(7), pp.1706-1711 (2014).
[20] Yang, F., Sambles, J.R. and Bradberry, G.W., "Long-range surface modes supported by thin films," Physical Review B, 44(11), p.5855 (1991).
[21] Chiadini, F., Fiumara, V., Scaglione, A. and Lakhtakia, A., "Composite surface-plasmon-polariton waves guided by a thin metal layer sandwiched between a homogeneous isotropic dielectric material and a periodically multilayered isotropic dielectric material," Journal of Nanophotonics, 9(1), p.093060 (2015).
[22] Chiadini, F., Fiumara, V., Scaglione, A. and Lakhtakia, A., "Compound surface-plasmon-polariton waves guided by a thin metal layer sandwiched between a homogeneous isotropic dielectric material and a structurally chiral material," Opt. Commun. 363, 201–206 (2016).
[23] Yeh, P., Yariv, A. and Hong, C.S., "Electromagnetic propagation in periodic stratified media. I. General theory," J. Opt. Soc. Am., 67(4), pp.423-438 (1977).
[24] Lakhtakia, A. and Polo Jr, J.A., "Dyakonov-Tamm wave at the planar interface of a chiral sculptured thin film and an isotropic dielectric material," arXiv preprint arXiv:0706.4287 (2007).
[25] Chiadini, F., Fiumara, V., Scaglione, A. and Lakhtakia, A., "Compound guided waves that mix characteristics of surface-plasmon-polariton, Tamm, Dyakonov–Tamm, and Uller–Zenneck waves," J. Opt. Soc. Am. B, 33(6), pp.1197-1206, (2016).
[26] Yeh, P., Yariv, A. and Cho, A.Y., "Optical surface waves in periodic layered media," Applied Physics Letters, 32(2), pp.104-105 (1978).
[27] Faryad, M., Hall, A. S., Barber, G. D., Mallouk, T. E., and Lakhtakia, A., "Excitation of multiple surface-plasmon-polariton waves guided by the periodically corrugated interface of a metal and a periodic multilayered isotropic dielectric material," J. Opt. Soc. Am. B 29, 704–713 (2012).
[28] Jaluria, Y., *Computer Methods for Engineering*, Taylor & Francis, (1996).
[29] Yakubovich, V. A., and Starzhinskii, V. M., *Linear Differential Equation with Periodic Coefficient* Wiley, New York (1975).
[30] J. A. Polo, Jr., T. G. Mackay and A. Lakhtakia, Electromagnetic surface waves: a Modern Perspective (Elsevier, 2013).
[31] Rasheed, M. and Faryad, M., "Excitation of the Uller-Zenneck electromagnetic surface waves in the prism-coupled configuration," Physical Review A, 96(2), p.023810 (2017).
[32] Jun Gao, Akhlesh Lakhtakia, John A. Polo, Jr. and Mangkai Lei, "Dyakonov-Tamm wave guided by a twist-defect in a structurally chiral material," JOSA A, 26 (7), p.1615, (2009).
[33] Maab, H. and Faryad, M., "Coupled Tamm waves guided by an isotropic and homogeneous dielectric layer in a rugate filter," Journal of Modern Optics, 61(12), pp.986-993 (2014).
[34] Maab, H., Faryad, M. and Lakhtakia, A., "Surface electromagnetic waves supported by the interface of two semi-infinite rugate filters with sinusoidal refractive-index profiles," J. Opt. Soc. Am. B, 28(5), pp.1204-1212 (2011).